

# Low-Frequency Current Fluctuations in Quasi-1D (TaSe<sub>4</sub>)<sub>2</sub>I Weyl Semimetal Nanoribbons

Subhajit Ghosh, Fariborz Kargar, Nick R. Sesing, Zahra Barani, Tina T. Salguero, Dong Yan, Sergey Rumyantsev, and Alexander A. Balandin\*

Low-frequency current fluctuations, i.e., electronic noise, in quasi-1D (TaSe<sub>4</sub>)<sub>2</sub>I Weyl semimetal nanoribbons are discussed. It is found that the noise spectral density is of the  $1/f$  type and scales with the square of the current,  $S_I \sim I^2$  ( $f$  is the frequency). The noise spectral density increases by almost an order of magnitude and develops Lorentzian features near the temperature  $T \approx 225$  K. These spectral changes are attributed to the charge-density-wave phase transition even though the temperature of the noise maximum deviates from the reported Peierls transition temperature in bulk (TaSe<sub>4</sub>)<sub>2</sub>I crystals. The noise level, normalized by the channel area, in these Weyl semimetal nanoribbons is surprisingly low,  $\approx 10^{-9} \mu\text{m}^2 \text{Hz}^{-1}$  at  $f = 10$  Hz, when measured below and above the Peierls transition temperature. The obtained results shed light on the specifics of electron transport in quasi-1D topological Weyl semimetals and can be important for their proposed applications as downscaled interconnects.

quasi-1D material is defined as a Weyl semimetal with Weyl points located above and below the Fermi level, forming pairs with the opposite chiral charge. At temperatures below the Peierls transition temperature  $T_p = 248\text{--}263$  K, (TaSe<sub>4</sub>)<sub>2</sub>I reveals the charge-density-wave (CDW) phase.<sup>[4,8–13]</sup> The quantum CDW phase consists of a periodic modulation of the electronic charge density accompanied by a periodic distortion of the atomic lattice.<sup>[14–19]</sup> It has been suggested that (TaSe<sub>4</sub>)<sub>2</sub>I reveals a correlated topological phase, which arises from the formation of CDW in a Weyl semimetal.<sup>[11,12]</sup> This quasi-1D quantum material represents an interesting avenue for exploring the interplay of correlations and topology, as well as being an exciting system for examining new functionalities and electronic applications.<sup>[17,20]</sup>

## 1. Introduction

Recently, 1D van der Waals (vdW) quantum materials with emergent topological phases, derived from strongly correlated interactions, have attracted significant attention.<sup>[1–3]</sup> A prototype example is a tetra-selenide compound (TaSe<sub>4</sub>)<sub>2</sub>I, with a structure featuring unusual axially chiral (TaSe<sub>4</sub>)<sub>n</sub> chains.<sup>[4–7]</sup> This

There are interesting applied physics and electronic materials aspects in the research of topological semimetals. The resistance and current density bottlenecks in downscaled metal interconnect motivate the search for new materials for the back end of the line (BEOL) interconnect applications.<sup>[21,22]</sup> When the interconnect linewidth scales below the electron mean free path, its resistivity increases in a power-law function due to


S. Ghosh, F. Kargar, Z. Barani, A. A. Balandin  
Nano-Device Laboratory  
Department of Electrical and Computer Engineering  
Bourns College of Engineering  
University of California, Riverside  
Riverside, CA 92521, USA  
E-mail: balandin@ece.ucr.edu

S. Ghosh, F. Kargar, Z. Barani, A. A. Balandin  
Phonon Optimized Engineered Materials Center  
Bourns College of Engineering  
University of California, Riverside  
Riverside, CA 92521, USA

N. R. Sesing, T. T. Salguero  
Department of Chemistry  
University of Georgia  
Athens, GA 30602, USA

D. Yan  
Center for Nanoscale Science and Engineering  
University of California, Riverside  
Riverside, CA 92521, USA

S. Rumyantsev  
CENTERA Laboratories  
Institute of High-Pressure Physics  
Polish Academy of Sciences  
Warsaw 01–142, Poland

 The ORCID identification number(s) for the author(s) of this article can be found under <https://doi.org/10.1002/aelm.202200860>.

© 2022 The Authors. Advanced Electronic Materials published by Wiley-VCH GmbH. This is an open access article under the terms of the Creative Commons Attribution License, which permits use, distribution and reproduction in any medium, provided the original work is properly cited.

DOI: 10.1002/aelm.202200860

increased electron scattering from interfaces and grain boundaries.<sup>[23,24]</sup> This problem is persistent for all elemental metals, including Cu, Co, and Ru. Quasi-1D vdW materials demonstrated different dependencies where the resistivity remained nearly constant with the scaling of the interconnect cross-sectional area due to their single-crystal nature and sharp vdW boundary interfaces.<sup>[25,26]</sup> There are indications that in some topological semimetals, the electrical conductivity can increase as the cross-sectional area decreases. Recent studies have shown that in the topological Weyl semimetal NbAs the resistivity can decrease by an order of magnitude from 35  $\mu\Omega$  cm in bulk single crystals to 1–5  $\mu\Omega$  cm in  $\approx$ 200 nm nanoribbons.<sup>[27]</sup> For this reason, a better understanding of electron transport phenomena in Weyl semimetals can have an immediate practical significance for interconnect applications.<sup>[28,29]</sup>

Here, we report on the low-frequency current fluctuations, i.e., low-frequency electronic noise, also referred to as excess noise, in  $(\text{TaSe}_4)_2\text{I}$  nanoribbons. The low-frequency noise includes the  $1/f$  and generation–recombination (G–R) noise with a Lorentzian-type spectrum, which comes on top of the thermal and shot noise background ( $f$  is the frequency). It is known that  $1/f$  noise can provide information on the electron transport and charge carrier recombination in a given material, as well as serve as an early indicator of electromigration damage.<sup>[30–35]</sup> We have previously used low-frequency noise measurements for monitoring phase transition in various materials<sup>[36–39]</sup> as well as for assessing the material quality and device reliability.<sup>[40–42]</sup> In this work, we are primarily motivated by the following questions. Is electron transport in the topological Weyl semimetals characterized by inherently lower noise owing to the suppression of certain electron scattering channels? Can one use the excess noise data to verify the CDW transitions in the topological Weyl semimetals? We are also interested in assessing if Weyl semimetals are acceptable for interconnect applications in terms of their electronic noise level.

## 2. Experimental Section

The crystal structure of quasi-1D  $(\text{TaSe}_4)_2\text{I}$  above  $T_p$  is illustrated in **Figure 1a** with a view showing  $(\text{TaSe}_4)_n$  chains aligned along the  $c$ -axis, within an iodide lattice.<sup>[43]</sup> The view of a single  $(\text{TaSe}_4)_n$  chain highlights several key features, including the coordination of each Ta center to eight selenium atoms in rectangular antiprismatic geometry, the equidistant Ta centers at  $\approx$ 3.2 Å that support metallic bonding, the slightly asymmetric bridging of  $\text{Se}_2^{2-}$  pairs between Ta centers, in part due to interactions with iodide, and most notably, the rotating pattern of  $\text{Se}_2^{2-}$  about the chain axis that generates axial chirality. Single crystal  $(\text{TaSe}_4)_2\text{I}$  source materials were synthesized by the chemical vapor transport (CVT) method from stoichiometric amounts of tantalum and selenium, and an excess of iodine that serves as both reactant and transport agent. Using a temperature gradient of 590–530 °C provided mm- to cm-sized  $(\text{TaSe}_4)_2\text{I}$  crystals in good yield. Complete preparative details are provided in the Supplementary Information.<sup>[19,44]</sup>

The quality of this material was examined using several methods (see **Figure 1b,c**). Scanning electron microscopy (SEM) reveals features exhibited by many 1D van der Waals

materials, such as growth striations and facile cleavage along the van der Waals gap. Powder X-ray diffraction (PXRD) data were collected on a Bruker D8 Advance instrument utilizing a  $\text{Co-K}\alpha$  X-ray source ( $\lambda = 1.78890$  Å) operated at 35 kV and 40 mA. Data were collected from 10° to 80°  $2\theta$  with a scan rate of 0.1 s per step. Samples were prepared as ground powder mounts. Powder X-ray diffraction (XRD) confirms the structure of  $(\text{TaSe}_4)_2\text{I}$ . Energy-dispersive X-ray spectroscopy (EDS) demonstrates homogeneity and provides the composition of the material. Some selenium and iodide deficiencies are well-known for metal chalcogenide compounds and are expected here.<sup>[45,46]</sup> The details of PXRD, SEM, EDS, and composition are provided in the Supporting Information.

The quasi-1D nanoribbons of  $(\text{TaSe}_4)_2\text{I}$  were prepared using a mechanical exfoliation technique on top of clean Si/SiO<sub>2</sub> substrates (University Wafer, p-type Si/SiO<sub>2</sub>, <100>). Here, we use the term nanoribbon rather than nanowire to describe these structures because the width of the selected structures was substantially wider than the thickness. This allowed for more accurate nanofabrication, testing, and comparison with quasi-2D materials. The exfoliated  $(\text{TaSe}_4)_2\text{I}$  nanoribbons had a length of a few micrometers, a width on the scale of hundred nanometers, and a thickness in the range of 10–100 nm as confirmed by atomic force microscopy (AFM). The AFM images for two exfoliated nanoribbons with different thicknesses are shown in **Figure 2a**. A representative Raman spectrum of the exfoliated nanoribbons is provided in **Figure 2b**. One can clearly see seven Raman peaks at the frequencies of 63.9, 67.9, 100.1, 143.3, 160.3, 182.8, and 270.9  $\text{cm}^{-1}$ , in line with prior reports on bulk  $(\text{TaSe}_4)_2\text{I}$  crystals.<sup>[47–50]</sup> All observed Raman frequencies belong to the A<sub>1</sub> vibrational mode type, except the peak at 67.9  $\text{cm}^{-1}$  which belongs to the B<sub>2</sub> symmetry group.<sup>[48]</sup> The test structures with multiple electrodes were prepared using electron-beam lithography (EBL) to define the contacts on the same nanoribbon. Electron beam evaporation (EBE) was used to deposit Cr/Au metals (10 nm/100 nm) to form the contacts for measurements. **Figure 2c** shows a schematic of the test structure, containing several metal contacts and pads on the Si/SiO<sub>2</sub> substrate. The channel lengths of the individual devices, i.e., the distance between two contacts, were in the range of 1–6  $\mu\text{m}$ . The quality of the contacts and the nanoribbon channels was verified with SEM. A colored SEM image of a representative  $(\text{TaSe}_4)_2\text{I}$  nanoribbon test structure is provided in **Figure 2d**.

The temperature-dependent current–voltage ( $I$ – $V$ ) measurements of the fabricated nanoribbon test structures were carried out inside a cryogenic probe station (Lakeshore TTPX) under vacuum using a semiconductor analyzer (Agilent B1500). The low-frequency noise measurements were performed using an in-house-built system. The noise measurement circuit consists of a low-noise DC battery, a potentiometer (POT), and a load resistor connected in series to the device under test (DUT) kept inside the probe station chamber. The POT controls the voltage drops between the load and the DUT of the voltage divider noise circuit. The load resistor was kept grounded in this configuration. During the noise measurements, the voltage fluctuations at the output were transferred to a low noise pre-amplifier (SR-560) which amplified the signal and sent it to a signal analyzer. The signal analyzer transformed the time domain signal to its corresponding frequency domain. In our

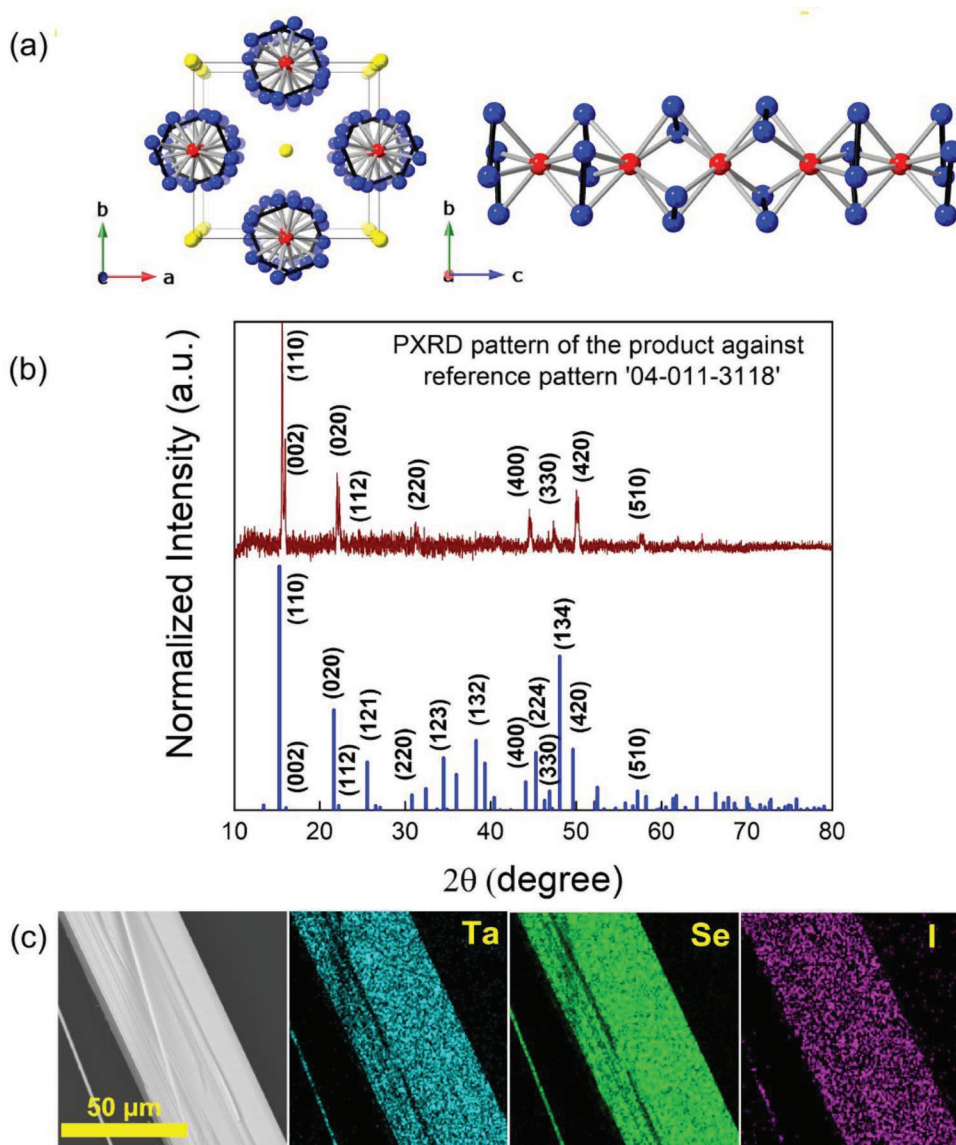


**Figure 1.** a) Crystal structure of  $(\text{TaSe}_4)_2\text{I}$  viewed down the *c*-axis (left panel) and a single chain of  $[\text{TaSe}_4]$  viewed down the *a*-axis (right panel), with atoms corresponding to Ta (red), Se (blue), and I (yellow). b) Powder X-ray diffraction pattern of the CVT-grown crystals; experimental (top) and reference card 04-011-3118 (bottom pattern). c) Scanning electron microscopy image of a mechanically exfoliated  $(\text{TaSe}_4)_2\text{I}$  crystal surface and corresponding energy-dispersive spectroscopy elemental mapping.

noise calculations, the voltage spectral density,  $S_V$ , was recalculated to its equivalent current spectral density,  $S_I$ , and normalized by the corresponding current squared,  $I^2$ . Further details of our noise measurement systems and procedures can be found in the Supporting Information and the prior reports for other materials and devices.<sup>[39,40,51,52]</sup>

To study the electrical characteristics of low-dimensional materials, which reveal phase transitions, it is important to verify the quality of the electrical contacts. **Figure 3a** presents the low-bias  $I$ - $V$  characteristics of one of the  $(\text{TaSe}_4)_2\text{I}$  test structures for several channel lengths, i.e.,  $I$ - $V$ s measured between different pairs of contacts. The  $I$ - $V$ s show linear behavior across the measured bias ranges confirming high-quality Ohmic contacts. The contact resistance of  $(\text{TaSe}_4)_2\text{I}$  nanoribbon was

determined using the conventional transmission line measurement (TLM) technique (see **Figure 3b**). The contact resistance value for this representative device, with a channel thickness of 28.5 nm, was determined to be  $2R_C = 440 \Omega$ , which is an order of magnitude lower than any of the channel resistances,  $R$ . The latter further confirms the quality of the fabricated contacts. The fact that  $R_C \ll R$  is beneficial for the interpretation of the noise measurements as well. More information on contact resistance can be found in the Supporting Information.

The as-measured low-frequency voltage noise spectral density,  $S_V$ , is shown in **Figure 3c**. The room-temperature data are presented for a  $(\text{TaSe}_4)_2\text{I}$  nanoribbon device with the 2  $\mu\text{m}$  channel length measured for the source-drain bias,  $V_D$ , ranging from 10 to 60 mV. The noise spectra for all bias voltages are of



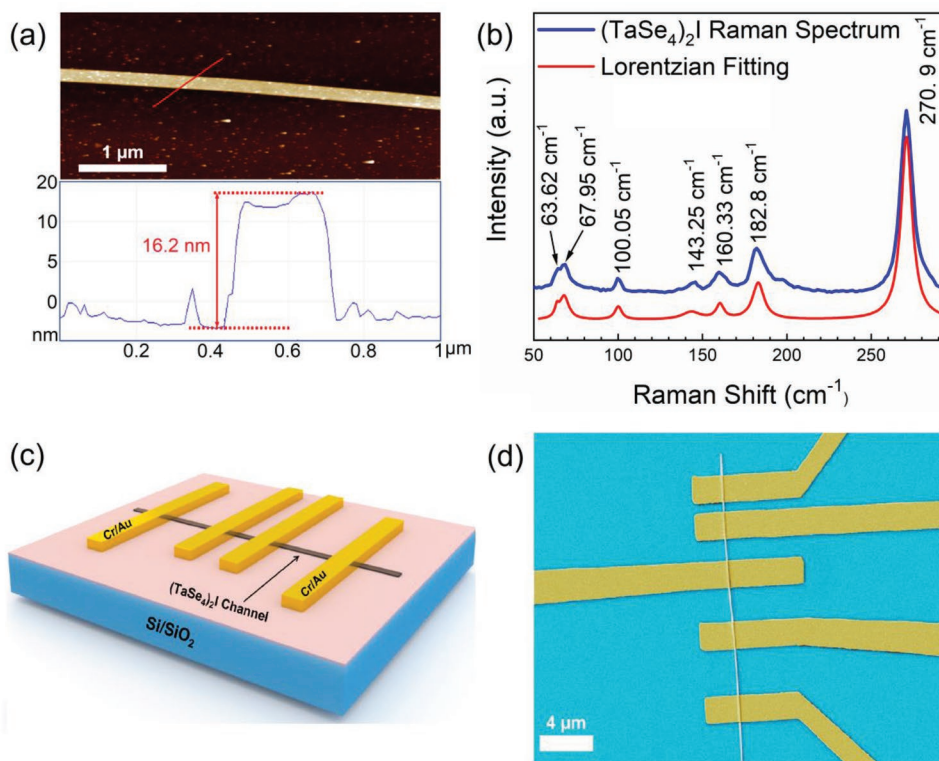


**Figure 2.** Characterization of the exfoliated quasi-1D  $(\text{TaSe}_4)_2\text{I}$  nanoribbons. a) Atomic force microscopy image of a representative exfoliated nanoribbon. b) Raman spectrum of a  $(\text{TaSe}_4)_2\text{I}$  nanoribbon at room temperature. c) Schematic of a  $(\text{TaSe}_4)_2\text{I}$  nanoribbon test structure on Si/SiO<sub>2</sub> substrate. d) Scanning electron microscopy image of a  $(\text{TaSe}_4)_2\text{I}$  nanoribbon test structure with varying channel lengths from 1 to 4  $\mu\text{m}$ . Pseudo-colors are used for clarity.

$1/f^\gamma$  ( $\gamma \approx 1$ ) flicker noise type, which is typical for both semiconductor and metallic materials.<sup>[30,38,39,53]</sup> The noise level measured at the lowest bias point is at least an order of magnitude higher than the background noise of the measurement system, confirming that the flicker  $1/f$  noise is intrinsic to the DUT and not from any other source. The corresponding current spectral density,  $S_I$ , as a function of the source–drain current,  $I$ , at a fixed frequency of  $f = 10$  Hz is presented in Figure 3d. The  $S_I$  versus  $I$  behavior is quadratic, i.e.,  $S_I \sim I^2$ , with an exact slope of 1.98. The quadratic scaling of the noise spectral density,  $S_I$ , with the source–drain current is expected for any linear resistor. Thus, we verified the accuracy of the noise measurement procedures and the fact that the  $(\text{TaSe}_4)_2\text{I}$  nanoribbons act as passive linear resistors.

### 3. Results and Discussions

The temperature-dependent  $I$ – $V$ s and noise data for a  $(\text{TaSe}_4)_2\text{I}$  device with a 2  $\mu\text{m}$  channel length are presented in Figure 4a–d (refer to the Supporting Information for the  $I$ – $V$  data of a different  $(\text{TaSe}_4)_2\text{I}$  nanoribbon device). Figure 4a shows the device resistance in a logarithmic scale normalized by the resistance of the channel at 300 K, i.e.,  $\log[R/R_{300}]$ , as a function of the inverse temperature, i.e.,  $10^3/T$ . The  $I$ – $V$  measurements were conducted both in the heating and cooling cycles. Overall, the dependence of the  $\log[R/R_{300}]$  on inverse temperature is

consistent with prior reports for bulk  $(\text{TaSe}_4)_2\text{I}$  samples.<sup>[4,5,8–13]</sup> There is a change in the slope of the resistance below RT. This slope change is more clearly observed in the plot of the derivative characteristics presented in Figure 4b. In our case, we observed the transition at  $T = 235$  K for both cooling and heating cycle measurements. Previous reports attributed the change in the resistivity slope to the Peierls transition, i.e., CDW phase transition, observed mostly at  $T_p = 260$ – $263$  K.<sup>[4,8,9]</sup> However, some reports indicated this transition at a temperature as low as  $T_p = 235$ – $240$  K.<sup>[54,55]</sup> It is known from experience with other CDW materials, that the temperature of the CDW phase transition may depend on the sample thickness.<sup>[56,57]</sup> In addition, some data scatter for the transition temperature can be due to small stoichiometric variations, e.g., the loss of iodine or selenide deficiency.

It has been stated that the Peierls transition in  $(\text{TaSe}_4)_2\text{I}$  is accompanied by opening a CDW energy bandgap of  $\approx 0.2$  eV.<sup>[4,12,58,59]</sup> There is an unusual feature of the phase transition in  $(\text{TaSe}_4)_2\text{I}$ , which was noticed and discussed in the original studies of bulk crystals.<sup>[8–10]</sup> The material reveals a non-metallic  $R(T)$  dependence both below and above  $T_p$ . This issue was addressed in detail in a report that described  $(\text{TaSe}_4)_2\text{I}$  as the zero-bandgap semiconductor and introduced a notion of the semiconductor–semiconductor phase transition.<sup>[58]</sup> In our measurements with  $(\text{TaSe}_4)_2\text{I}$  nanoribbons, the resistance change near  $T_p$  is consistently observed but it is somewhat more gradual than in the case of bulk samples. We speculate that this can be

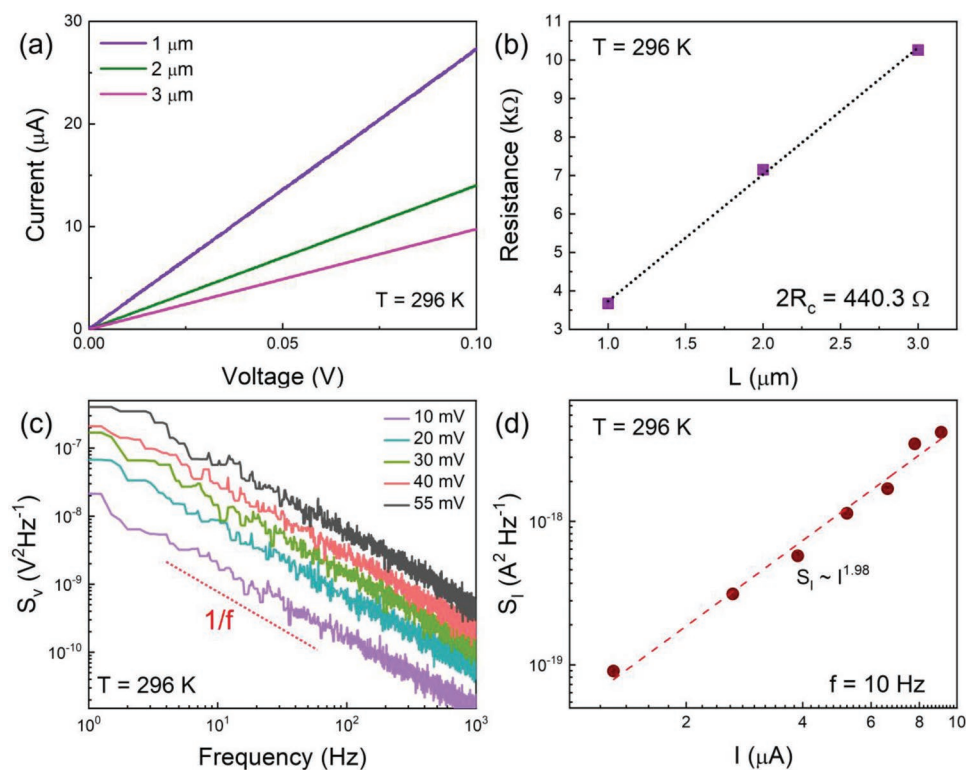


**Figure 3.** Electrical and low-frequency noise characteristics of a  $(\text{TaSe}_4)_2\text{I}$  nanoribbons at room temperature. a) Current–voltage characteristics for nanoribbon devices with different channel lengths. b) Resistance of the nanoribbon devices as a function of the channel lengths. c) Voltage noise spectral density,  $S_v$ , as a function of frequency for a  $(\text{TaSe}_4)_2\text{I}$  nanoribbon device at different source–drain biases. d) Current noise spectral density,  $S_i$ , as a function of the device current.

related to the strain induced by the lattice mismatch between the material and  $\text{Si}/\text{SiO}_2$  substrate. The latter is supported by our experiments with  $\text{Al}_2\text{O}_3$  and other substrates and prior reports on the effect of the substrate-induced strain on resistive switching in nanowires.<sup>[13,60–62]</sup> Based on the above considerations, we can conclude that our measured resistivity dependence on temperature is in line with previous reports,<sup>[8–11,13]</sup> and focus on the current fluctuations in  $(\text{TaSe}_4)_2\text{I}$  nanoribbons.

Figure 4c shows the normalized noise current spectral density,  $S_i/I^2$ , as a function of frequency,  $f$ , at temperatures near  $T_p$  for the same device. The noise measurements were conducted between 200 and 235 K to capture the Peierls transition from a possible change in the noise spectrum. One can notice an evolution of the  $1/f$  spectrum to Lorentzian bulge near the Peierls transition temperature. To clarify the trend, we plotted  $f \times S_i/I^2$  versus  $f$ , which removes the  $1/f$  background. One can see that at  $T = 225$  K, the noise spectral density reaches a maximum and develops a Lorentzian bulge. As the temperature increases further the noise becomes  $1/f$  again, and its level decreases. We argue that the noise increase and Lorentzian feature are signatures of the Peierls transition, which we observed in the resistivity behavior in Figure 4a,b. The same trend—noise increases and Lorentzian-type bulges near the CDW phase transitions has been reported previously for different materials.<sup>[36–39]</sup> Some differences in temperature  $T_p$  extracted from the resistivity and noise data can be explained by a difference in the rate at which the temperature was changed in the probe station during these two independent measurements. In addition, there is a

possibility of a temperature drift during the noise measurements. Generally, the Lorentzian noise spectrum is a signature of a two-level system.<sup>[63,64]</sup> In the case of a phase transition, the material state and its resistance can switch between the two phases until the material system is driven further away from the transition point  $T_p$ . We observed similar behavior in  $1\text{T-TaS}_2$ , another CDW material.<sup>[36,37]</sup> It is unlikely that the Lorentzian bulges which we see in the noise spectrum of  $(\text{TaSe}_4)_2\text{I}$  are due to the generation–recombination (G–R) noise that originates from high concentrations of one type of defects with particular time constants since it is observed only at one temperature and the noise spectrum returns to its original  $1/f$  type.

In Figure 5a, we provide a comparison of the electrical and noise characteristics near the phase transition point on the same plot. The data attest to the potential of noise spectroscopy for monitoring phase transitions. In Figure 5b, we plot the noise spectral density normalized for the channel area,  $\beta = S_i/I^2 \times (W \times L)$ , at a fixed frequency  $f = 10$  Hz and two representative values of the current. We have previously introduced the  $\beta$  parameter to compare low-frequency noise levels in 2D materials such as graphene and  $\text{MoS}_2$ .<sup>[65,66]</sup> One can see that the noise spectral density increases by an order of magnitude near  $T_p$  proving that the excess noise level is a suitable indicator of the phase transition. Figure 5b also indicates the low noise level, normalized by the channel area, in  $(\text{TaSe}_4)_2\text{I}$  nanoribbons compared to 2D materials. The nanoribbon shape of the  $(\text{TaSe}_4)_2\text{I}$  channels, with a width much larger than the thickness, makes the comparison with 2D materials meaningful. The value

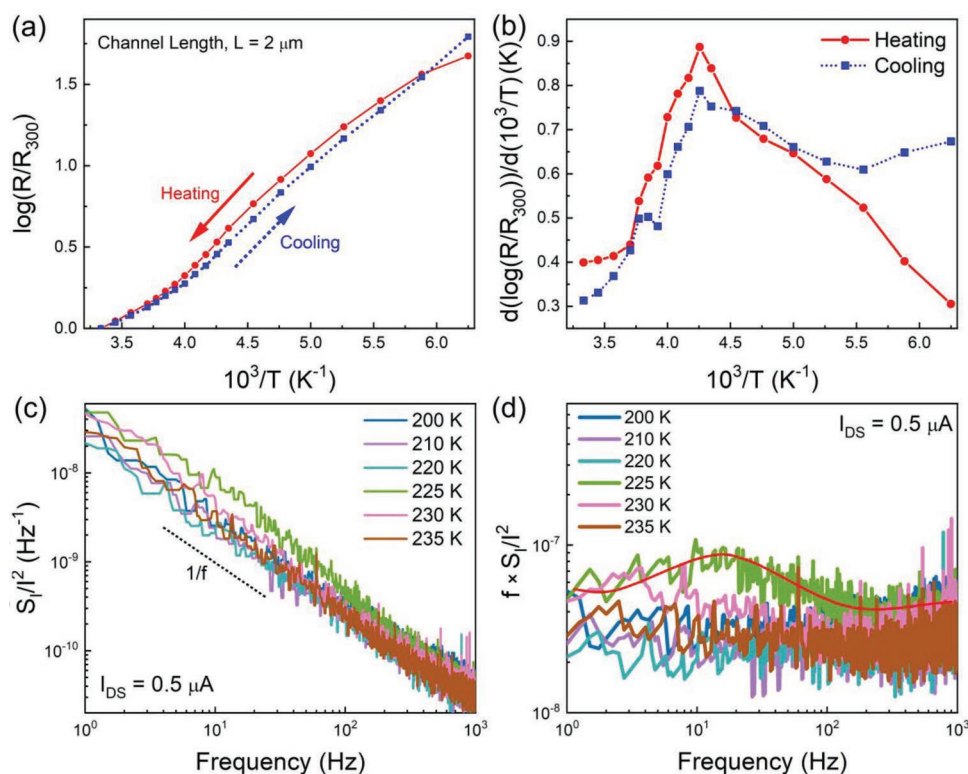


**Figure 4.** Temperature-dependent electrical and low-frequency noise characteristics of a  $(\text{TaSe}_4)_2\text{I}$  nanoribbon device. a) Logarithmic normalized resistance,  $\log(R/R_{300})$ , as a function of inverse temperature,  $10^3/T$ , for a  $(\text{TaSe}_4)_2\text{I}$  nanoribbon device with a 2- $\mu\text{m}$  channel length. b) Logarithmic derivative,  $d(\log(R/R_{300}))/d(10^3/T)$ , versus inverse temperature of the same device. c) Normalized noise current spectral density,  $S_I/I^2$ , as a function of frequency at temperatures near the transition temperature measured at a constant device current of 0.5  $\mu\text{A}$ . The noise behavior is of  $1/f$  type, except at  $T = 225$  K, where the noise becomes Lorentzian type. d) Normalized noise spectral density multiplied by the frequency,  $f \times S_I/I^2$ , as a function of frequency at different temperatures.

of the  $\beta$  parameter away from the phase transition is below  $2 \times 10^{-9} \mu\text{m}^2 \text{Hz}^{-1}$  ( $f = 10$  Hz). For comparison, the area-normalized noise level in graphene is  $\beta = 10^{-8} \mu\text{m}^2 \text{Hz}^{-1}$  while that in thin  $\text{MoS}_2$  is  $\beta = 10^{-5} \mu\text{m}^2 \text{Hz}^{-1}$ .<sup>[65]</sup> The noise level,  $S_I/I^2$ , without surface normalization, is also rather low, below  $4 \times 10^{-9} \text{Hz}^{-1}$  ( $f = 10$  Hz), away from the phase transition point, both in the low and high-temperature regions. The noise level reported for nanoribbons of  $\text{ZrTe}_3$  was in the range of  $10^{-9}$  to  $10^{-8}$  ( $f = 10$  Hz).<sup>[18,67]</sup> Unfortunately, the direct comparison of the noise levels in different quasi-1D and 2D materials is not always possible since the tested structure sizes are often not reported, and one cannot do the normalization by the channel area. Additional electrical and noise characterization data are provided in the Supporting Information.

One can envision two possible reasons for a rather small level of noise in the nanoribbons of quasi-1D or quasi-2D vdW materials. It is known that the van der Waals bonding may result in a smaller number of surface dangling bonds.<sup>[25,30]</sup> The latter can lead to the suppression of some scattering processes and, correspondingly, to lower noise levels. On the other side,  $(\text{TaSe}_4)_2\text{I}$  is also a topological semimetal. This means that some electron scattering is suppressed due to the topologically protected conduction states. It is not possible to state at this point if the low level of noise in  $(\text{TaSe}_4)_2\text{I}$  nanoribbons is due to the current fluctuation suppression in the topologically protected conductive channels of the Weyl semimetal.<sup>[68–70]</sup> The latter

would require a dedicated theoretical study allowing to connect the electron scattering and capture rates with the fluctuations in the number of electrons and their mobility. The experimental data reported in this study indicate an unexpectedly low noise level and motivate future studies. We also note that the noise level measured in this Weyl semimetal nanoribbons is sufficiently low for interconnect applications.

The resistivity extracted for these nanoribbons was similar to the values reported for bulk  $(\text{TaSe}_4)_2\text{I}$ , on the order of  $\approx 10^{-3} \Omega \text{cm}$ .<sup>[9,11]</sup> Previous studies reported that in some topological semimetals, the resistivity can decrease with the decreasing cross-sectional area of the conductors.<sup>[27–29,70]</sup> In our present study, the resistivity values that we obtained for nanoribbons of different sizes were not sufficient to claim the specific trend with the cross-section area within the standard error of the measurements. It was recently reported that annealing, i.e., due to heating or passing current, can improve the current conduction in thinner films of topological semimetals.<sup>[71]</sup> One should be able to exclude this effect from the topological scattering suppression. We reserve such a systematic study for future work. The investigated  $(\text{TaSe}_4)_2\text{I}$  vdW material may not be the optimum one for interconnect applications in terms of its resistivity, but the low noise level for topological Weyl semimetals is a promising feature. It is known that low-frequency noise can be an early indicator of damage to materials and devices.<sup>[72–75]</sup> With the device degradation, the



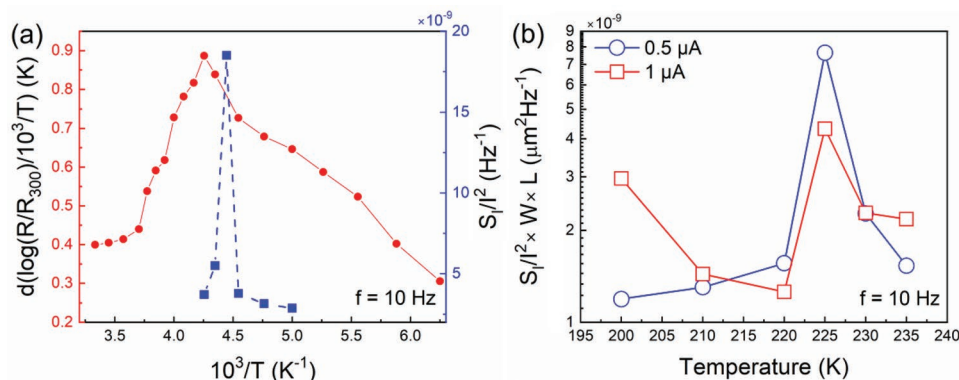


**Figure 5.** Comparison of the electrical and noise characteristics near the phase transition point. a) The derivative of the resistance (red curve) with the corresponding noise spectral density (blue curve) measured at  $f = 10$  Hz. The phase transition point can be established from both the maximum of the resistance derivative and the noise spectral density. A slight deviation between the maxima of the electrical and noise characteristics can be attributed to the difference in the rate at which the temperature was changed during these two independent measurements. b) The evolution of the normalized noise spectral density with the temperature at different current levels. The noise spectral density normalized by device current and channel area,  $S_I/I^2 \times W \times L$ , measured at  $f = 10$  Hz, at the constant currents of  $I_{DS} = 0.5$  and  $1.0 \mu\text{A}$ . The noise level increases substantially near the transition temperature  $T \approx 225$  K.

noise increases at a much faster rate than the changes in the averaged characteristics such as  $I$ - $V$ s. The latter makes the noise a sensitive predictor of a lifetime. The results obtained in this work can be used for developing assessment methodologies for the reliability of topological semimetals.

## 4. Conclusion

We have described low-frequency current fluctuations in quasi-1D  $(\text{TaSe}_4)_2\text{I}$  Weyl semimetal nanoribbons. The noise spectral density increases by almost an order of magnitude and develops Lorentzian features near the temperature  $T \approx 225$  K. These spectral changes were attributed to the CDW phase transition even though the temperature of the noise maximum deviates from the reported Peierls transition temperature in bulk crystals. The noise level normalized to the device area in the Weyl semimetal nanowires was found to be surprisingly low,  $S_I/I^2 \times (W \times L) \approx 10^{-9} \text{ Hz}^{-1}$  at  $f = 10$  Hz, when measured below and above the Peierls transition temperature. This value is an order of magnitude lower than that in graphene and other quasi-2D materials. These results shed light on the specifics of electron transport in quasi-1D topological Weyl semimetals and can be important for their proposed applications as downscaled interconnects.

## Supporting Information

Supporting Information is available from the Wiley Online Library or from the author.

## Acknowledgements

A.A.B. was supported by the Vannevar Bush Faculty Fellowship from the Office of Secretary of Defense (OSD) under the Office of Naval Research (ONR) contract N00014-21-1-2947. The work of T.T.S. and N.R.S. was supported by the subcontract of this ONR award. A.A.B. also

acknowledges the support from the National Science Foundation (NSF) program Designing Materials to Revolutionize and Engineer the Future (DMREF) via a project DMR-1921958 entitled Collaborative Research: Data-Driven Discovery of Synthesis Pathways and Distinguishing Electronic Phenomena of 1D van der Waals Bonded Solids. S.R. was supported, in part, by the International Research Agendas program of the Foundation for Polish Science co-financed by the European Union under the European Regional Development Fund No. MAB/2018/9.

## Conflict of Interest

The authors declare no conflict of interest.

## Author Contributions

A.A.B. conceived the idea, coordinated the project, and led the experimental data analysis and manuscript preparation. S.G. fabricated the test structures, performed Raman spectroscopy, measured  $I$ - $V$ s, and electronic noise characteristics, and contributed to data analysis. N.R.S. synthesized the bulk crystals and conducted material characterization. T.T.S. supervised material synthesis and contributed to material data analysis. Z.B. assisted with Raman spectroscopy and contributed to material characterization. D.Y. assisted with cleanroom nanofabrication. S.R. and F.K. contributed to the noise data analysis. All authors contributed to the manuscript preparation.

## Data Availability Statement

The data that support the findings of this study are available from the corresponding author upon reasonable request.

## Keywords

$1/f$  noise, charge-density-waves, nanoribbons, topological semimetals, Weyl semimetals

Received: July 31, 2022  
Revised: October 11, 2022  
Published online:

- [1] Y. Yuan, W. Wang, Y. Zhou, X. Chen, C. Gu, C. An, Y. Zhou, B. Zhang, C. Chen, R. Zhang, Z. Yang, *Adv. Electron. Mater.* **2020**, *6*, 1901260.
- [2] O. F. Shoron, M. Goyal, B. Guo, D. A. Kealhofer, T. Schumann, S. Stemmer, *Adv. Electron. Mater.* **2020**, *6*, 2000676.
- [3] I. D. Bernardo, J. Hellerstedt, C. Liu, G. Akhgar, W. Wu, S. A. Yang, D. Culcer, S. K. Mo, S. Adam, M. T. Edmonds, M. S. Fuhrer, *Adv. Mater.* **2021**, *33*, 2005897.
- [4] J. Gooth, B. Bradlyn, S. Honnali, C. Schindler, N. Kumar, J. Noky, Y. Qi, C. Shekhar, Y. Sun, Z. Wang, B. A. Bernevig, C. Felser, *Nature* **2019**, *575*, 315.
- [5] A. A. Sinchenko, R. Ballou, J. E. Lorenzo, T. Grenet, P. Monceau, *Appl. Phys. Lett.* **2022**, *120*, 063102.
- [6] W. Shi, B. J. Wieder, H. L. Meyerheim, Y. Sun, Y. Zhang, Y. Li, L. Shen, Y. Qi, L. Yang, J. Jena, P. Werner, K. Koepfner, S. Parkin, Y. Chen, C. Felser, B. A. Bernevig, Z. Wang, *Nat. Phys.* **2021**, *17*, 381.
- [7] T. Konstantinova, L. Wu, W. G. Yin, J. Tao, G. D. Gu, X. J. Wang, J. Yang, I. A. Zaloznyak, Y. Zhu, *npj Quantum Mater.* **2020**, *5*, 80.
- [8] M. Maki, M. Kaiser, A. Zettl, G. Grüner, *Solid State Commun.* **1983**, *46*, 497.
- [9] Z. Z. Wang, M. C. Saint-Lager, P. Monceau, M. Renard, P. Gressier, A. Meerschaut, L. Guemas, J. Rouxel, *Solid State Commun.* **1983**, *46*, 325.
- [10] H. Fujishita, M. Sato, S. Hoshino, *Solid State Commun.* **1984**, *49*, 313.
- [11] I. A. Cohn, S. G. Zytsev, A. P. Orlov, S. v. Zaitsev-Zotov, *JETP Lett.* **2020**, *112*, 88.
- [12] X. P. Li, K. Deng, B. Fu, Y. K. Li, D. S. Ma, J. F. Han, J. Zhou, S. Zhou, Y. Yao, *Phys. Rev. B* **2021**, *103*, L081402.
- [13] Q. G. Mu, D. Neno, Y. P. Qi, F. R. Fan, C. Pei, M. Elghazali, J. Gooth, C. Felser, P. Narang, S. Medvedev, *Phys. Rev. Mater.* **2021**, *5*, 084201.
- [14] G. Grüner, *Rev. Mod. Phys.* **1988**, *60*, 1129.
- [15] S. v. Zaitsev-Zotov, *Phys.-Usp.* **2004**, *47*, 533.
- [16] P. Monceau, *Adv. Phys.* **2012**, *61*, 325.
- [17] A. A. Balandin, S. v. Zaitsev-Zotov, G. Grüner, *Appl. Phys. Lett.* **2021**, *119*, 170401.
- [18] V. Favre-Nicolin, S. Bos, J. E. Lorenzo, J.-L. Hodeau, J.-F. Berar, P. Monceau, R. Currat, F. Levy, H. Berger, *Phys. Rev. Lett.* **2001**, *87*, 015502.
- [19] S. V. Smaalen, E. J. Lam, J. Lüdecke, *J. Phys.: Condens. Matter* **2001**, *13*, 9923.
- [20] A. A. Balandin, F. Kargar, T. T. Salguero, R. K. Lake, *Mater. Today* **2022**, *55*, 74.
- [21] Z. Chen, N. Boyajian, Z. Lin, R. T. Yin, S. N. Obaid, J. Tian, J. A. Brennan, S. W. Chen, A. N. Miniovich, L. Lin, Y. Qi, X. Liu, I. R. Efimov, L. Lu, *Adv. Mater. Technol.* **2021**, *6*, 2100225.
- [22] A. Ruiz-Clavijo, O. Caballero-Calero, D. Navas, A. A. Ordoñez-Cencerrado, J. Blanco-Portals, F. Peiró, R. Sanz, M. Martín-González, *Adv. Electron. Mater.* **2022**, *8*, 2200342.
- [23] W. Steinhögl, G. Schindler, G. Steinlesberger, M. Engelhardt, *Phys. Rev. B* **2002**, *66*, 075414.
- [24] D. Josell, S. H. Brongersma, Z. Tokei, *Ann. Rev. Mater.* **2009**, *39*, 231.
- [25] M. A. Stolyarov, G. Liu, M. A. Bloodgood, E. Aytan, C. Jiang, R. Samnakay, T. T. Salguero, D. L. Nika, S. L. Rumyantsev, M. S. Shur, K. N. Bozhilov, A. A. Balandin, *Nanoscale* **2016**, *8*, 15774.
- [26] T. A. Empante, A. Martinez, M. Wurch, Y. Zhu, A. K. Geremew, K. Yamaguchi, M. Isarraraz, S. Rumyantsev, E. J. Reed, A. A. Balandin, L. Bartels, *Nano Lett.* **2019**, *19*, 4355.
- [27] C. Zhang, Z. Ni, J. Zhang, X. Yuan, Y. Liu, Y. Zou, Z. Liao, Y. Du, A. Narayan, H. Zhang, T. Gu, X. Zhu, L. Pi, S. Sanvito, X. Han, J. Zou, Y. Shi, X. Wan, S. Y. Savrasov, F. Xiu, *Nat. Mater.* **2019**, *18*, 482.
- [28] C. T. Chen, U. Bajpai, N. A. Lanzillo, C. H. Hsu, H. Lin, G. Liang, Technical Digest – International Electron Devices Meeting, *IEDM* **2020**, 32.4.1.
- [29] D. Gall, J. J. Cha, Z. Chen, H. J. Han, C. Hinkle, J. A. Robinson, R. Sundaraman, R. Torsi, *MRS Bull.* **2021**, *46*, 959.
- [30] G. Liu, S. Rumyantsev, M. A. Bloodgood, T. T. Salguero, M. Shur, A. A. Balandin, *Nano Lett.* **2017**, *17*, 377.
- [31] S. Beyne, K. Croes, I. de Wolf, Z. Tokei, *J. Appl. Phys.* **2016**, *119*, 184302.
- [32] T. M. Chen, A. M. Yassine, *IEEE Trans. Electron Devices* **1994**, *41*, 2165.
- [33] B. Neri, A. Diligenti, P. E. Bagnoli, *IEEE Trans. Electron Devices* **1987**, *34*, 2317.
- [34] P. Dutta, P. M. Horn, *Rev. Mod. Phys.* **1981**, *53*, 497.
- [35] W. Yang, Z. Çelik-Butler, *Solid-State Electron.* **1991**, *34*, 911.
- [36] G. Liu, S. Rumyantsev, M. A. Bloodgood, T. T. Salguero, A. A. Balandin, *Nano Lett.* **2018**, *18*, 3630.
- [37] R. Salgado, A. Mohammadzadeh, F. Kargar, A. Geremew, C. Y. Huang, M. A. Bloodgood, S. Rumyantsev, T. T. Salguero, A. A. Balandin, *Appl. Phys. Express* **2019**, *12*, 037001.
- [38] A. K. Geremew, S. Rumyantsev, F. Kargar, B. Debnath, A. Nosek, M. A. Bloodgood, M. Bockrath, T. T. Salguero, R. K. Lake, A. A. Balandin, *ACS Nano* **2019**, *13*, 7231.
- [39] S. Ghosh, F. Kargar, A. Mohammadzadeh, S. Rumyantsev, A. A. Balandin, *Adv. Electron. Mater.* **2021**, *7*, 2100408.
- [40] S. Ghosh, K. Fu, F. Kargar, S. Rumyantsev, Y. Zhao, A. A. Balandin, *Appl. Phys. Lett.* **2021**, *119*, 243505.
- [41] S. Ghosh, H. Surdi, F. Kargar, F. A. Koeck, S. Rumyantsev, S. Goodnick, R. J. Nemanich, A. A. Balandin, *Appl. Phys. Lett.* **2022**, *120*, 062103.
- [42] R. Samnakay, A. A. Balandin, P. Srinivasan, *Solid-State Electron.* **2017**, *135*, 37.
- [43] P. Gressier, L. Guemas, A. Meerschaut, *Acta Crystallogr.* **1982**, *38*, 2877.
- [44] P. Gressier, A. Meerschaut, L. Guemas, J. Rouxel, P. Monceau, *J. Solid State Chem.* **1984**, *51*, 141.
- [45] H. Yi, Z. Huang, W. Shi, L. Min, R. Wu, C. M. Polley, R. Zhang, Y. F. Zhao, L. J. Zhou, J. Adell, X. Gui, W. Xie, M. H. W. Chan, Z. Mao, Z. Wang, W. Wu, C. Z. Chang, *Phys. Rev. Res.* **2021**, *3*, 013271.
- [46] F. Kargar, A. Krayev, M. Wurch, Y. Ghafouri, T. Debnath, D. Wickramaratne, T. T. Salguero, R. K. Lake, L. Bartels, A. A. Balandin, *Nanoscale* **2022**, *14*, 6133.
- [47] I. Ohana, D. Schmeltzer, D. Shaltiel, Y. Yacoby, A. Mustachi, *Solid State Commun.* **1985**, *54*, 747.
- [48] A. Zwick, M. A. Renucci, P. Gressier, A. Meerschaut, *Solid State Commun.* **1985**, *56*, 947.
- [49] S. Sugai, M. Sato, S. Kurihara, *Phys. Rev. B* **1985**, *32*, 6809.
- [50] T. Sekine, T. Seino, M. Izumi, E. Matsuura, *Solid State Commun.* **1985**, *53*, 767.
- [51] A. K. Geremew, S. Rumyantsev, M. A. Bloodgood, T. T. Salguero, A. A. Balandin, *Nanoscale* **2018**, *10*, 19749.
- [52] A. Geremew, C. Qian, A. Abelson, S. Rumyantsev, F. Kargar, M. Law, A. A. Balandin, *Nanoscale* **2019**, *11*, 20171.
- [53] A. A. Balandin, *Nat. Nanotechnol.* **2013**, *8*, 549.
- [54] S. M. Shapiro, M. Sato, S. Hoshino, *J. Phys.: Condens. Matter* **1986**, *19*, 4709.
- [55] M. Saint-Paul, P. Monceau, F. Lévy, *Solid State Commun.* **1988**, *67*, 581.
- [56] P. Goli, J. Khan, D. Wickramaratne, R. K. Lake, A. A. Balandin, *Nano Lett.* **2012**, *12*, 5941.
- [57] R. Samnakay, D. Wickramaratne, T. R. Pope, R. K. Lake, T. T. Salguero, A. A. Balandin, *Nano Lett.* **2015**, *15*, 2965.
- [58] C. Tournier-Colletta, L. Moreschini, G. Autès, S. Moser, A. Crepaldi, H. Berger, A. L. Walter, K. S. Kim, A. Bostwick, P. Monceau, E. Rotenberg, O. v. Yazyev, M. Grioni, *Phys. Rev. Lett.* **2013**, *110*, 236401.
- [59] Z. Huang, H. Yi, L. Min, Z. Mao, C. Z. Chang, W. Wu, *Phys. Rev. B* **2021**, *104*, 205138.



- [60] J. Wu, Q. Gu, B. S. Guiton, N. P. de Leon, L. Ouyang, H. Park, *Nano Lett.* **2006**, 6, 2313.
- [61] H. M. Lefcochilos-Fogelquist, O. R. Albertini, A. Y. Liu, *Phys. Rev. B* **2019**, 99, 174113.
- [62] M. K. Lin, J. A. Hlevyack, P. Chen, R. Y. Liu, S. K. Mo, T. C. Chiang, *Phys. Rev. Lett.* **2020**, 125, 176405.
- [63] D. J. Ulness, A. C. Albrecht, *Phys. Rev. A* **1996**, 53, 1081.
- [64] T. Grasser, *Noise in Nanoscale Semiconductor Devices*, Springer Nature, Cham, Switzerland **2020**.
- [65] S. L. Romyantsev, C. Jiang, R. Samnakay, M. S. Shur, A. A. Balandin, *IEEE Electron Device Lett.* **2015**, 36, 517.
- [66] M. A. Stolyarov, G. Liu, S. L. Romyantsev, M. Shur, A. A. Balandin, *Appl. Phys. Lett.* **2015**, 107, 023106.
- [67] A. Geremew, M. A. Bloodgood, E. Aytan, B. W. K. Woo, S. R. Corber, G. Liu, K. Bozhilov, T. T. Salguero, S. Romyantsev, M. P. Rao, A. A. Balandin, *IEEE Electron Device Lett.* **2018**, 39, 735.
- [68] S. Y. Xu, N. Alidoust, I. Belopolski, Z. Yuan, G. Bian, T. R. Chang, H. Zheng, V. N. Strocov, D. S. Sanchez, G. Chang, C. Zhang, D. Mou, Y. Wu, L. Huang, C. C. Lee, S. M. Huang, B. Wang, A. Bansil, H. T. Jeng, T. Neupert, A. Kaminski, H. Lin, S. Jia, M. Z. Hasan, *Nat. Phys.* **2015**, 11, 748.
- [69] M. Z. Hasan, G. Chang, I. Belopolski, G. Bian, S. Y. Xu, J. X. Yin, *Nat. Rev. Mater.* **2021**, 6, 784.
- [70] L. Qiao, X. Xiong, H. Yang, D. Chen, Y. Li, J. Li, X. Peng, Z. Xu, J. Han, W. Xiao, Y. Yao, *J. Phys. Chem. C* **2021**, 125, 22312.
- [71] A. Fereidouni, M. H. Doha, K. Pandey, R. Basnet, J. Hu, H. O. H. Churchill, *Appl. Phys. Lett.* **2022**, 121, 113101.
- [72] L. K. J. Vandamme, *IEEE Trans. Electron Devices* **1994**, 41, 2176.
- [73] J. Xu, D. Abbott, Y. Dai, *Microelectron. Reliab.* **2000**, 40, 171.
- [74] Z. Gingl, C. Pennetta, L. B. Kiss, L. Reggiani, *Semicond. Sci. Technol.* **1996**, 11, 1770.
- [75] A. A. Balandin, *Noise and Fluctuations Control in Electronic Devices*, American Scientific Publishers, USA **2002**, p. 258.